Laser-assisted modern nuclear physics

T.E. Cocolios
STFC Ernest Rutherford Fellow
School of Physics and Astronomy, The University of Manchester

Ecole Joliot-Curie on
Experimental Techniques in Modern Nuclear Physics
28 September - 2 October 2015

Contents

Chapter 1

Preamble

When I was asked to lecture at the Joliot-Curie, I was both excited and frightened. It is a big honour, but also a big task. The subject topic, *lasers for nuclear stuff*, is broad and vague enough that I could take it down any path I thought appropriate. I have had to make editorial decisions along the way and I hope that the readers will still gain a reasonable overview of the field of interest.

I thus decided to provide the participants with a general overview of the field, with enough theoretical insight to understand where the different concepts come from, where they meet, where they differ. It is always difficult to gauge what is enough input from having too many equations, so in the end the reader is better referred to reference text books for the detailed derivations.

On the experimental notes, it is once again difficult to give everybody a fair share of the cake without dividing it into too many crumbs. A choice has to be made somewhere. Those who feel spoiled in the process should come and let me know; this can be settled with a drink and a staring contest.

These lecture notes are a new endeavour and might be prone to the risk associated with any new project: typographical errors, especially in formulae, incomplete information, ... This is very much a project in progress and should be taken as such.

Enjoy and feel free to let me know if you spot anything!

TEC

Chapter 2

From the atom to the nucleus

This chapter is dedicated to the theoretical premises of relevance to the discussions further in these lecture notes. Basics of quantum mechanics will be introduced to reveal how the study of the atom can reveal a lot of information on the nature of the atomic nucleus. The full derivations can be lengthy and are best left to external references, such as your favourite quantum mechanics books. Only the skeleton of the derivation will be provided here in an attempt to highlight the relevant components to the discussion.

2.1 Atomic levels

To first order, the atom can be represented as a positive point-like core with Z charges surrounded by negatively charged electrons (see Fig. 2.1). An electron is then subject to the Coulomb potential of the central charge (referred to, for simplicity, as the *nucleus*)

$$V(r) = \frac{Ze^2}{4\pi\epsilon_0 r}, \tag{2.1}$$

where r is the distance of the electron from the nucleus. For simplicity, we shall discuss first a single-electron system, otherwise known as hydrogen-like. The Schrödinger equation for such an electron is then written as

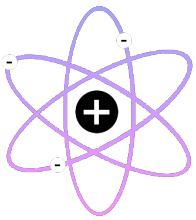

Figure 2.1: Artistic representation of the atom.

$$\left(-\frac{\hbar}{2m}\nabla^2 + V \right)\psi = E\psi. \tag{2.2}$$

Since $V = V(r)$, this equation is best solved in spherical coordinates. Since $V(r)$ is independent of the angular coordinates, it is possible to separate the variables of the wavefunction as

$$\psi(r, \theta, \phi) = R(r)Y(\theta, \phi). \tag{2.3}$$

Eq. 2.2 can then be rewritten into two separate equations, using a cleverly inspired choice of separation variable, $l(l+1)$:

$$\frac{1}{R(r)}\frac{d}{dr}\left(r^2\frac{d}{dr}\right)R(r) - \frac{2mr^2}{\hbar^2}\big[V(r) - E\big] = l(l+1), \tag{2.4}$$

$$\frac{1}{Y(\theta,\phi)\sin\theta}\frac{\partial}{\partial\theta}\left(\sin\theta\frac{\partial}{\partial\theta}\right)Y(\theta,\phi) + \frac{1}{Y(\theta,\phi)\sin^2\theta}\frac{\partial^2}{\partial\phi^2}Y(\theta,\phi) = -l(l+1). \tag{2.5}$$

Eq. 2.3 can further be separated between the polar and azimuthal components using

$$Y(\theta, \phi) = f(\theta)g(\phi) \tag{2.6}$$

and choosing m^2 as the separation variable[1], Eq. 2.5 becomes

$$\frac{\sin\theta}{f(\theta)}\frac{d}{d\theta}\left(\sin\theta\frac{d}{d\theta}\right)f(\theta) + l(l+1)\sin^2\theta = m^2 \quad \& \tag{2.7}$$

$$\frac{1}{g(\phi)}\frac{d^2}{d\phi^2}g(\phi) = -m^2. \tag{2.8}$$

Eq. 2.4, 2.7, and 2.8 are solved on backwards from their present order. The azimuthal Eq. 2.8 gives

$$g_m(\phi) = e^{im\phi}, \tag{2.9}$$

which is true for any value of m. The polar Eq. 2.7 is solved by the associated Legendre polynomials $P_{l,m}(x)$, which are only defined provided that l is a non-negative integer and that $|m| \leq l$.

$$f_{l,m}(\theta) = (-1)^m\sqrt{\frac{(2l+1)(l-m)!}{4\pi(l+m)!}}P_{l,m}(\cos\theta), \tag{2.10}$$

$$\text{where} \quad l \in \mathbb{N} \quad \& \quad |m| \leq l. \tag{2.11}$$

[1]This value is not related to the mass m that was written in Eq. 2.2 and 2.4

Table 2.1: Number of electrons occupying the different orbitals.

	$l=0$ $j=\frac{1}{2}$	$l=1$ $j=1/2,3/2$	$l=2$ $j=3/2,5/2$	$l=3$ $j=5/2,7/2$	Cumulated number	Magic element
$n=1$	2	-	-	-	2	He
$n=2$	2	6	-	-	10	Ne
$n=3$	2	6	10	-	28	Ni
$n=4$	2	6	10	14	42	Mo

Finally, the radial Eq. 2.4 is solved by the associated Laguerre polynomials $L_q^k(x)$, where $q, k \in \mathbb{N}$ and $k \leq q$. After much work, one can eventually show that

$$R_{n,l}(r) = \sqrt{\frac{2}{na_0}^3 \frac{(n-l-1)!}{2n\big[(n+l)!\big]^3}} e^{-r/na_0} \left(\frac{2r}{na_0}\right)^l L_{n-l-1}^{2l+1}\left(\frac{2r}{na_0}\right), \tag{2.12}$$

$$\text{where} \quad n \in \mathbb{N} \quad \& \quad n \geq l+1 \tag{2.13}$$

and a_0 is the Bohr atom radius.

From this mathematical description of a single electron in the Coulomb field of an atomic nucleus, we immediately see the atomic level structure appearing as

$$\text{Principal quantisation} \qquad n = 1, 2, 3, \ldots \tag{2.14}$$

$$\text{Angular momentum} \qquad l = 0, \ldots, n-1 \tag{2.15}$$

$$\text{Magnetic substate} \qquad m = -l, \ldots, 0, \ldots, l \tag{2.16}$$

The final ingredient to get a complete picture of the atom is the spin of the electron, which couples to the angular momentum l to give a total angular momentum j, and allows for two magnetic substates with $\pm 1/2$ units of angular momentum, hereby doubling the number of available states. This last ingredient is introduced perturbatively into the Hamiltonian, and the splitting of the states is referred to as the *fine structure of the atom*.

$$\text{Total angular momentum} \quad j = l \pm \frac{1}{2}, \quad j > 0. \tag{2.17}$$

When putting these conditions together, one gets a simple picture as an outcome, as seen in Table 2.1. Filling up all the orbitals with the same principal quantum number n results in ${}_2$He and ${}_{10}$Ne, both noble gases known to be very tightly bound, namely magical elements. Note that this picture breaks down quickly as the next expected magic element would be ${}_{28}$Ni, which is not a noble gas, and which means that we have overlooked ${}_{18}$Ar. The reason for this discrepancy is that the atom is a multiple-electron system and not a single-electron system, as derived above. The electrons will then provide an additional force onto each other, which results in some orbitals being more or less shielded than others from the nucleus. A reorganisation of the shells follows, from which the $4s$ shell will be filled before the $3d$ shell,

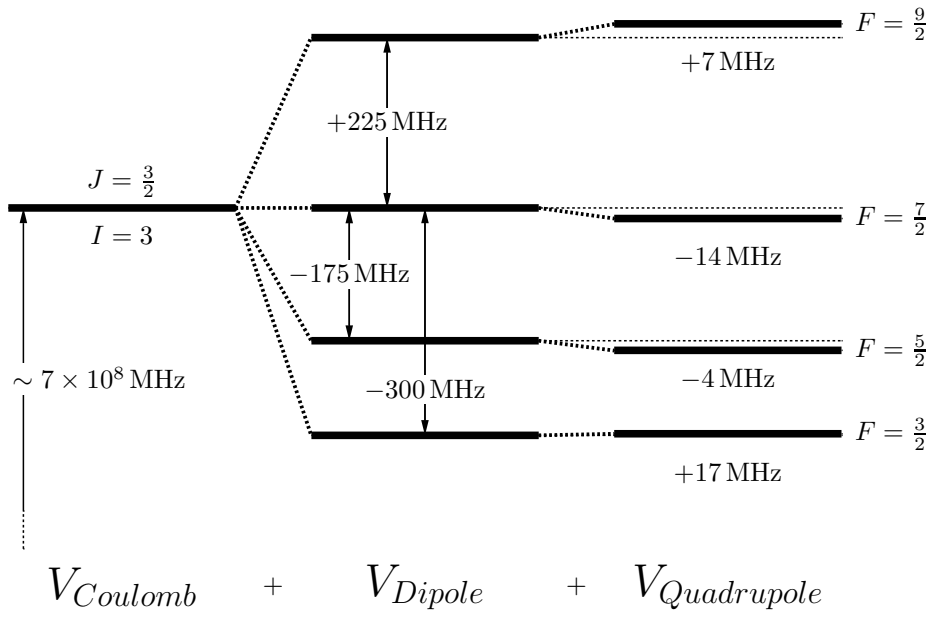

Figure 2.2: Hyperfine splittings of the $^8P_{3/2}$ state in $^{206g}_{87}$Fr.

making $_{18}$Ar magic, the $5s$ shell before the $4d$, making $_{36}$Kr magic, ... The different electrons also combine together towards making the total angular momentum of the atom, J; note that most of the electrons will pair two by two into a $J = 0$ pair, leaving the angular momentum to be determined by a few valence electrons.

2.2 The hyperfine structure of the atomic levels

The derivation above has been written assuming a point-like nucleus with a positive charge Ze. We know however that the nucleus has a finite size and the potential from Eq. 2.1 can be written as a multipole expansion as follows:

$$V(r) = V_{Coulomb}(r^{-1}) + V_{Dipole}(r^{-3}) + V_{Quadrupole}(r^{-5}) + \dots \tag{2.18}$$

Those perturbations are very small in magnitude and typically amount to a fraction of the fine structure splitting.

2.2.1 The magnetic dipole moment

Considering the fact that the nucleus has an angular momentum of spin I, it will have an associated magnetic moment μ, which will interact with the magnetic field B produced by the electron. This will produce a perturbation on the atomic levels according to the following Hamiltonian:

$$-\boldsymbol{\mu} \cdot \boldsymbol{B}. \tag{2.19}$$

The total angular momentum of the atomic system then needs to be rewritten to account for the total electron angular momentum and the nuclear spin into

$$\boldsymbol{F} = \boldsymbol{I} + \boldsymbol{J}, \tag{2.20}$$

$$\text{where} \quad |I - J| \leq F \leq I + J. \tag{2.21}$$

The energy of the atomic level is then shifted by

$$\Delta E = \frac{A}{2} K \tag{2.22}$$

$$\text{where} \quad A = \frac{\mu B_0}{IJ}, \tag{2.23}$$

$$\text{and} \quad K = F(F+1) - I(I+1) - J(J+1) \tag{2.24}$$

and B_0 is the magnitude of the magnetic field of the electron at the site of the nucleus.

Note that in the case that $I = 0$ or $J = 0$, there is no hyperfine structure and the atomic level remains a single level.

Spin determination with the hyperfine parameter A

One can immediately see that there are two parts to the hyperfine parameter A: an electronic component, $\frac{B_0}{J}$, and a nuclear component, $\frac{\mu}{I}$. While the value of B_0 might be difficult to calculate or measure experimentally, by measuring the hyperfine parameter across many isotopes, one has access to a relative measurement of μ as

$$\frac{A}{A'} = \frac{\mu B_0}{IJ} \frac{I'J}{\mu' B_0} = \frac{\mu I'}{\mu' I} \tag{2.25}$$

Thanks to alternative ways of measuring the absolute value of μ, such as βNMR, it is then possible to extract μ across all the isotopes of interest.

Another feature of the hyperfine splitting is its sensitivity to the nuclear spin I. The first means by which the hyperfine splitting may be used to identify the nuclear spin is by the number of hyperfine levels that are available. For $I = 0$, there are no sublevel, while for $I > 0$ there are many. Generally speaking there are $2I + 1$ sublevels, provided that $I \leq J$. Consequently, up to the limit of J, one may determine I simply from counting.

Furthermore, if one considers different states within a single atom, then the ratio of hyperfine parameters reduces to

$$\frac{A_1}{A_2} = \frac{\mu B_{01}}{IJ_1} \frac{IJ_2}{\mu B_{02}} = \frac{B_{01} J_2}{B_{02} J_1}, \tag{2.26}$$

which is independent of the specific isotope, and therefore a constant across the isotopic chain. The comparison of that ratio between a known isotope and one of unknown nuclear spin allows therefore the measurement of I.

The hyperfine anomaly

The discussion in the last paragraphs stems from the principles that the value of the magnetic field B_0 generated by the electron at the site of the nucleus is uniform over the nuclear volume and that the magnetisation distribution is as well. Neither of those principles are however valid, especially for large nuclei and low-l orbits, where a rapid change in the overlap of the magnetic field on the particle's wavefunction may be observed.

Instead, the interaction described in Eq. 2.19 must be averaged over the nuclear volume [Büt84]

$$A \to A(1+\epsilon), \tag{2.27}$$

and from the difference from one isotope to the next, Eq. 2.25 becomes

$$\frac{A}{A'} = \frac{\mu I'}{\mu' I}\frac{1+\epsilon}{1+\epsilon'} \approx \frac{\mu I'}{\mu' I}(1+\Delta'), \tag{2.28}$$

where Δ' is the hyperfine structure anomaly between the two isotopes, with typically $\Delta' < 1\%$. This parameter is in itself difficult to access as it requires the high precision measurement of the magnetic dipole moments and the hyperfine magnetic dipole parameters in both isotopes. Moreover, this parameter depends on the magnetic field B, which is a property of the atomic level of interest. No thorough investigation of the hyperfine anomaly has therefore ever been carried out and its use is anecdotic.

An approach that is considered is to see the impact of the hyperfine anomaly on Eq. 2.26:

$$\frac{A_1}{A_2} = \frac{B_{01}J_2}{B_{02}J_1}\frac{1+\epsilon_1}{1+\epsilon_2} \approx \frac{B_{01}J_2}{B_{02}J_1}(1+{}^1\Delta^2), \tag{2.29}$$

where ${}^1\Delta^2$ is the hyperfine structure anomaly between the two atomic levels within a given isotope, with typically ${}^1\Delta^2 < 1\%$.

2.2.2 The electric quadrupole moment

If the charge distribution of a nucleus is not spherically symmetric, it will exhibit an electric quadrupole moment Q. The perturbation associated with that uneven charge distribution will shift the atomic level energy by

$$\Delta E = \frac{B}{2}\frac{3K(K+1) - 2I(I+1)2J(J+1)}{2I(2I-1)2J(2J-1)} \tag{2.30}$$

$$\text{where} \quad B = \frac{eQ}{4}\frac{\partial^2 V}{\partial z^2}, \tag{2.31}$$

$$\tag{2.32}$$

and $\frac{\partial^2 V}{\partial z^2}$ is the gradient of the electric field of the electron at the site of the nucleus. The electric quadrupole moment is a perturbation on the perturbation and therefore has typically

a small impact on the hyperfine splitting of an atomic level. Any further multipole is even less relevant and will not be discussed in these lectures.

Note that in the case of $I = 0, \frac{1}{2}$ or $J = 0, \frac{1}{2}$, there is no electric quadrupole moment.

The combined effect of the magnetic dipole and electric quadrupole moments on an atomic level are illustrated in Fig. 2.2.

2.3 The transitions between atomic levels

2.3.1 State lifetime

The atomic population N_1 and N_2 between two energy levels E_1 and E_2 can be exchanged through an electromagnetic field of energy $h\nu = E_2 - E_1$, $E_2 > E_1$. This exchange is mediated by a photon at frequency ν and can proceed via three processes: *absorption*, *spontaneous emission*, and *induced emission*. The rate of change of the population in each level is then written as

$$-\frac{\mathrm{d}N_2}{\mathrm{d}t} = \frac{\mathrm{d}N_1}{\mathrm{d}t} = AN_2 - B_{12}\rho(\nu)N_1 + B_{21}\rho(\nu)N_2, \tag{2.33}$$

where A, B_{12}, and B_{21}[2] are the Einstein coefficients for spontaneous decay, absorption, and induced emission, and $\rho(\nu)$ is the energy density per unit frequency range of the radiation. In the absence of a field, $\rho(\nu) = 0$ and Eq. 2.33 becomes

$$\frac{\mathrm{d}N_2}{\mathrm{d}t} = -AN_2, \tag{2.34}$$

from which one extracts $N_2(t) = N_2(0)e^{-At}$, which means that the Einstein A coefficient is the reverse of the state partial lifetime τ. To extract the lifetime of a state, it is necessary to consider all the possible decays from that state to states E_i, such that $\tau = 1/\sum_i A_i$. It is also possible to relate the Einstein coefficients to each other as

$$A = \frac{8\pi\nu^2}{c^3}h\nu B_{21} = \frac{8\pi\nu^2}{c^3}h\nu\frac{g_1}{g_2}B_{12}, \tag{2.35}$$

where g_i is the degeneracy of state E_i.

2.3.2 Selection rules

The radiation field that connects the two atomic levels can be approximated, to first order, to an electric dipole field ($E1$): the photon carries 1 unit of angular momentum and the parity of the state changes. The following selection rules follow

[2]Those parameters are not related to the hyperfine parameters A and B.

$$\Delta l = \pm 1 \tag{2.36}$$
$$\Delta J = 0, \pm 1, \quad J = 0 \nrightarrow 0 \tag{2.37}$$
$$\Delta F = 0, \pm 1, \quad F = 0 \nrightarrow 0 \tag{2.38}$$

From Eq. 2.36, one determines that only transitions from $s \leftrightarrow p$, $p \leftrightarrow d$, $d \leftrightarrow f$, ... are possible.

From Eq. 2.37, this further restricts the range of states that can be linked to one another. At low energy in the atom, this may lead to the existence of *metastable states* which do not have any decay path to the ground state. Those states may then decay via first-forbidden decays, but the lifetime associated with those states is much higher than in the rest of the atom. Such states can be populated thermally, e.g., in the high temperature of an ion beam laser ion source (see section 3.1.1). They may also be on the possible decay path of an atomic state of interest in collinear laser spectroscopy or atom trapping, and are then referred to as *dark states*.

2.3.3 Relative amplitudes

If an atomic level has a hyperfine structure, then the transition from or to that level will be distributed over different frequencies. In the more general case, both levels will have a hyperfine structure and a set of transitions will be available, satisfying the selection rule from Eq. 2.38. Note that if the atomic transition validates already the selection rule from Eq. 2.37, there will be substates which validate that of Eq. 2.38.

Not all transitions will however be equivalent. The amplitude of a given transition will then be proportional to the matrix element joining one state to the other one under the action of the dipole radiation field:

$$\langle F_f, m_f | \boldsymbol{e} \cdot \boldsymbol{d} | F_i, m_i \rangle, \tag{2.39}$$

where $|F_i, m_i\rangle$ is the initial state and $|F_f, m_f\rangle$ is the final state. Applying the Wigner-Eckart theorem to separate out the $|F\rangle$ component and further decoupling the electron angular momentum J from the nuclear momentum I,[3] one obtains that the amplitude scales as

$$\big(2F_i + 1\big)\big(2F_j + 1\big) \begin{pmatrix} F_f & 1 & F_i \\ -m_f & 0 & m_i \end{pmatrix}^2 \begin{Bmatrix} J_f & F_f & I \\ F_i & J_i & 1 \end{Bmatrix}^2, \tag{2.40}$$

where $(\ldots)$ is a Wigner $3j$ symbol and $\{\ldots\}$ is a Wigner $6j$ symbol. These amplitudes involve the nuclear spin I directly in the Wigner $6j$ symbol, as well as indirectly through the different F values of the hyperfine states. The relative intensities of the hyperfine transitions

[3] I spare the reader the mathematical derivation but enthusiastically encourage the students to search for this enlightening derivation in their favourite reference book.

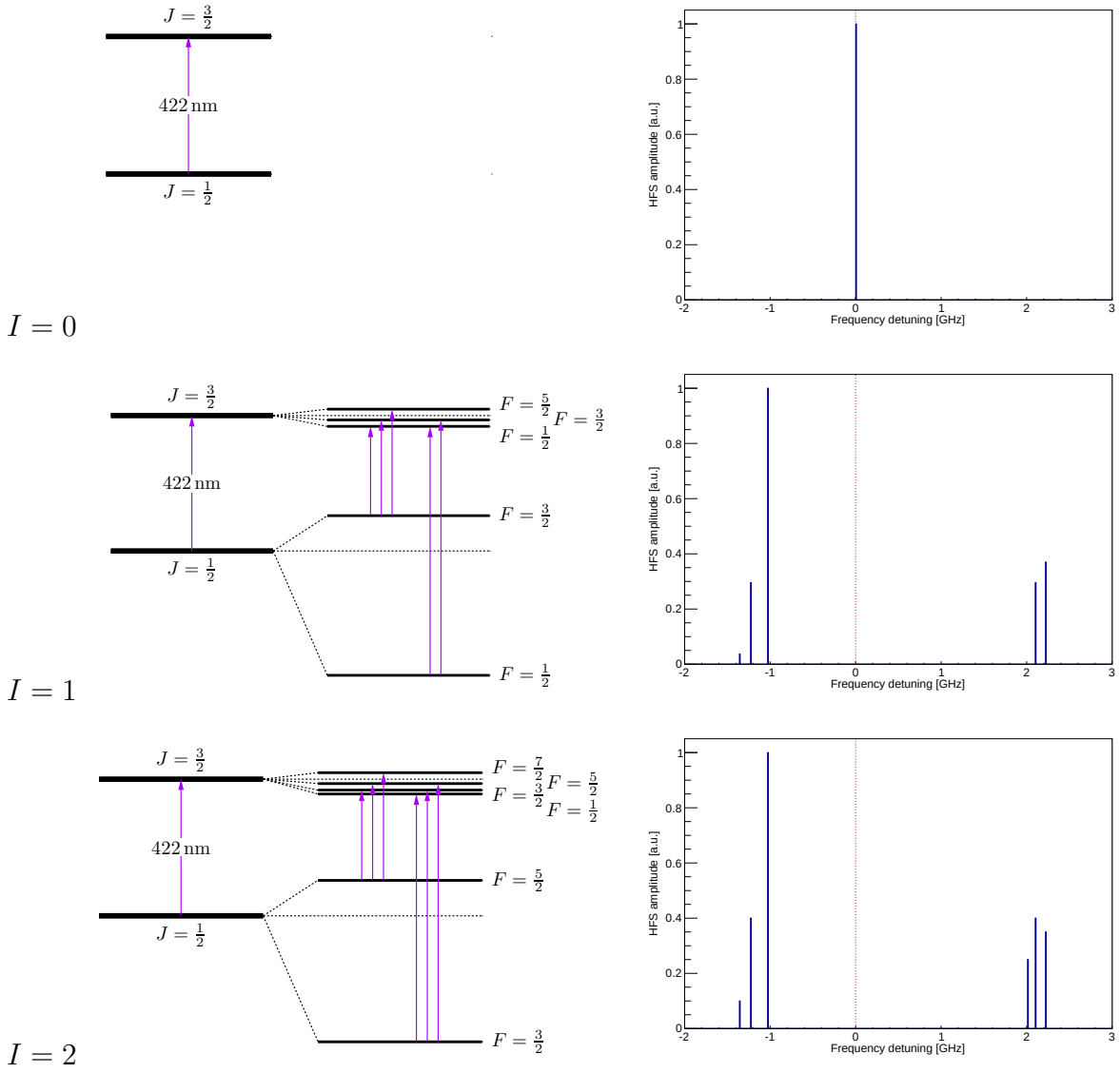

Figure 2.3: Simulated hyperfine structure for the $^7S_{1/2} \rightarrow ^8 P_{3/2}$ atomic transition in ^{214}Fr assuming nuclear spins $I = 0$ (top), $I = 1$ (middle) and $I = 2$ (bottom). For better display, the hyperfine parameter $A(^8P_{3/2})$ has been increased 10-fold. The number of peaks and their relative intensities show how the hyperfine structure can be used to measure the nuclear spin directly.

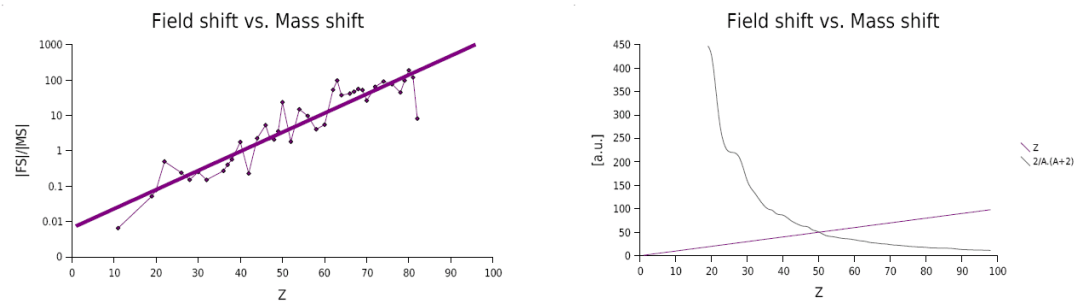

Figure 2.4: Comparing mass shifts and field shifts from selected atomic transitions across the periodic table. Left: data selected from [FH04]; Right: Trends in mass and field shifts normalised to cross at $Z = 47$.

of a given atomic transition will therefore change from one nuclear spin to the other and may be used as another way of measuring the nuclear spin in a nuclear-model independent way. An example of possible hyperfine intensities is shown in Fig. 2.3 to illustrate the difference between two nuclear spins.

There are two points over which one needs to be careful when using this approach. The first is that while the differences are very pronounced going from $I = 1$ to $I = 2$, the effect tends to wash out with increasing spin and it is nearly impossible to extract accurate spin information for the very high spins. Moreover, this derivation is very simple and assumes that the field is a perfect dipole with no additional perturbation. In practice, these criteria might not be fully met and a departure from these amplitudes may be observed, especially when using high power radiation fields or multiple transitions within the probing of the transition.

2.3.4 Isotope shift

Mass shift

When changing the number of neutrons from one isotope to the next of a given element, the charge of the nucleus, Ze, does not change. The properties described in section 2.1 are therefore unaffected, to first order. The change in the reduced mass of the system is however not negligible and affects each energy level differently. Moreover, as the atom is a multi-body system, the individual shift applied to each electron impacts the other energy levels as well. Altogether, when considering the frequency ν of a transition between two atomic levels, an isotope shift is observed as

$$\delta\nu^{AA'} = \frac{A' - A}{AA'}M, \tag{2.41}$$

where A and A' are the mass of each isotope in atomic mass units (amu) and M is an atomic parameter specific to a transition of an element. This atomic parameter is empirically split

into two contributions:

$$M = M_{NMS} + M_{SMS}, \tag{2.42}$$

referring to the *normal mass shift*, M_{NMS}, for the direct impact of the change in the reduced mass to the levels involved in the transition, and to the *specific mass shift*, M_{SMS}, for the impact that the rearranging of the atomic cloud has on the transition. M_{SMS} cannot be calculated analytically for a system with more than 3 electrons (Li-like systems) and one must rely on large-scale atomic calculations[4] [CCF12]. M_{NMS} is related to the transition frequency as

$$M_{NMS} = m_e \nu, \tag{2.43}$$

where m_e is the mass of the electron.

Note that the mass shift $\delta\nu^{AA'}$ scales as A^{-2}. Its relative importance will therefore be larger for light nuclei and becomes almost negligible in heavy systems. The value for M_{SMS} can also vary in sign, which can on the one hand cancel out with M_{NMS} and reduce M to almost 0, or alternatively can amplify the importance of the mass shift.

Field shift

In section 2.2, we have introduced the impact that the finite size of the nucleus has on the atomic level in terms of its magnetisation, uneven charge distribution, or even magnetisation distribution. There is however another impact, which is the fact that the charges themselves are distributed over a given volume. If the electron orbital overlaps with the nucleus, it will be affected differently when the nucleus changes size or exhibit deformation. This effect is called the volume effect, or *field shift*.

Only electrons in s and $p_{1/2}$ have a sizeable overlap with the nuclear volume and exhibit a measurable field shift. This therefore impacts atomic transitions involving such states, leading to the following isotope shift

$$\delta\nu = F\delta\langle r^2\rangle, \tag{2.44}$$

where F is an atomic parameter, which determination is as complex as that of M_{SMS}. To first order, however, this atomic parameters scales linearly with Z, making the field shift very important in heavy elements, in an opposite way to the mass shift. A comparison between mass and field shifts is presented in Fig. 2.4.

Additional corrections may apply to the field shift. One such correction is the involvement of higher radial moments, e.g., $\delta\langle r^4\rangle$. In that case, Eq. 2.44 becomes

$$\delta\nu = F\Lambda = F\big(\delta\langle r^2\rangle + C_4\delta\langle r^4\rangle + C_6\delta\langle r^6\rangle + \dots\big). \tag{2.45}$$

Those higher moments, also called the Seltzer moments, can be approximated to a fraction of $\delta\langle r^2\rangle$ and the appropriate scaling constants have been estimated for selected cases [Sel69].

[4]This issue has been the ground of an ECT* meeting in Trento, Italy, last August.

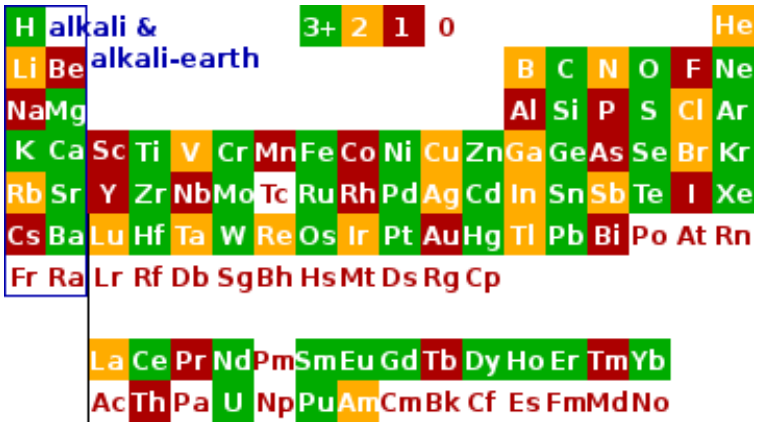

Figure 2.5: Periodic table showing the number of the number of stable/very-long-lived isotopes with which a target can be made for alternative charge radii studies.

This reduces Eq. 2.45 back to Eq. 2.44, with the adjustment that the proportionality constant F is no longer only the atomic parameter, but includes as well the correction factors for higher radial moments. Altogether, one may express the *total isotope shift* as

$$\delta\nu^{AA'} = \frac{A'-A}{AA'}\Big(m_e\nu + M_{SMS}\Big) + F\delta\langle r^2\rangle^{AA'}. \tag{2.46}$$

It is interesting to note that different nuclear states within a single isotope will have different nuclear properties, and therefore may have a different field shift, while the mass difference between two nuclear states is negligible on the same scale. In this case, the change in the atomic transition is referred to as the *isomer shift* and has the form of Eq. 2.44.

King plot

The main sources of systematic uncertainties in extracting $\delta\langle r^2\rangle$ from $\delta\nu$ are the atomic parameters M_{SMS} and F. Current state-of-the-art calculations only reach a precision of 1%, while the statistical uncertainties are much higher [DJS05, CCF12].

In order to reduce the impact of those parameters on the final nuclear observable, experimentally extracted atomic parameters are much more attractive. If a sufficient number of isotopes have been studied with alternative methods to measure $\delta\langle r^2\rangle$, such as electron scattering, muonic decays, or K x-ray studies, it is then possible to benchmark the isotope shift to those data according to the formalism of King.

Eq. 2.46 is normalised by a factor $\mu_{AA'} = \frac{AA'}{A'-A}$ in order to remove the mass dependence of the mass shift:

$$\mu_{AA'}\delta\nu^{AA'} = M + F\mu_{AA'}\delta\langle r^2\rangle^{AA'}. \tag{2.47}$$

Plotting $\mu_{AA'}\delta\langle r^2\rangle^{AA'}$ against $\mu_{AA'}\delta\nu^{AA'}$, also known as the *King plot*, should then produce a line, which slope is the total factor F (includes both the atomic and high-moment

contributions), and y-intercept is the total mass shift factor M. A minimum of 2 points is required to draw a line, and including the reference isotope A', a total of 3 isotopes at least need to be studied with the alternative method. These respective experiments have only been performed on stable isotopes so far, due to their limited cross sections. Fig. 2.5 shows which elements satisfy this condition. In the case that only 2 isotopes are available, a correlation between M and F can be determined.

Additional information can be gained from comparing different atomic transitions within the same element, with a formalism known as the *modified King plot* analysis. In this case, one starts from the principle that $\delta\langle r^2\rangle$ is independent of the atomic transition for a given nuclear state. Isolating for that term in Eq. 2.47 gives

$$\mu_{AA'}\delta\langle r^2\rangle^{AA'} = \frac{1}{F_1}\Big(\mu_{AA'}\delta\nu_1^{AA'} - M_1\Big) = \frac{1}{F_2}\Big(\mu_{AA'}\delta\nu_2^{AA'} - M_2,\Big) \tag{2.48}$$

where the subscript 1 and 2 refer to two different atomic transitions. The modified King plot is then the plot of $\mu_{AA'}\delta\nu_2^{AA'}$ against $\mu_{AA'}\delta\nu_1^{AA'}$ and will show a line, which slope is $\frac{F_2}{F_1}$ and which y-intercept is $M_2 - \frac{F_2}{F_1}M_1$. This allows to experimentally relate the atomic parameters of different transitions to one another over a wider range of isotopes than available for the standard King plot method. This approach can be used, for example, to test atomic calculations by comparing them to experimental observables, see e.g., [CDS$^+$11], or to extract the atomic parameters of a transition for which no atomic calculations are available, see e.g., [LBB$^+$14]. Examples of King and modified King plots are shown in Fig. 2.6.

$$\mu_{AA'}\delta\nu_2^{AA'} = \frac{F_2}{F_1}\mu_{AA'}\delta\nu_1^{AA'} + \left(M_2 - \frac{F_2}{F_1}M_1\right). \tag{2.49}$$

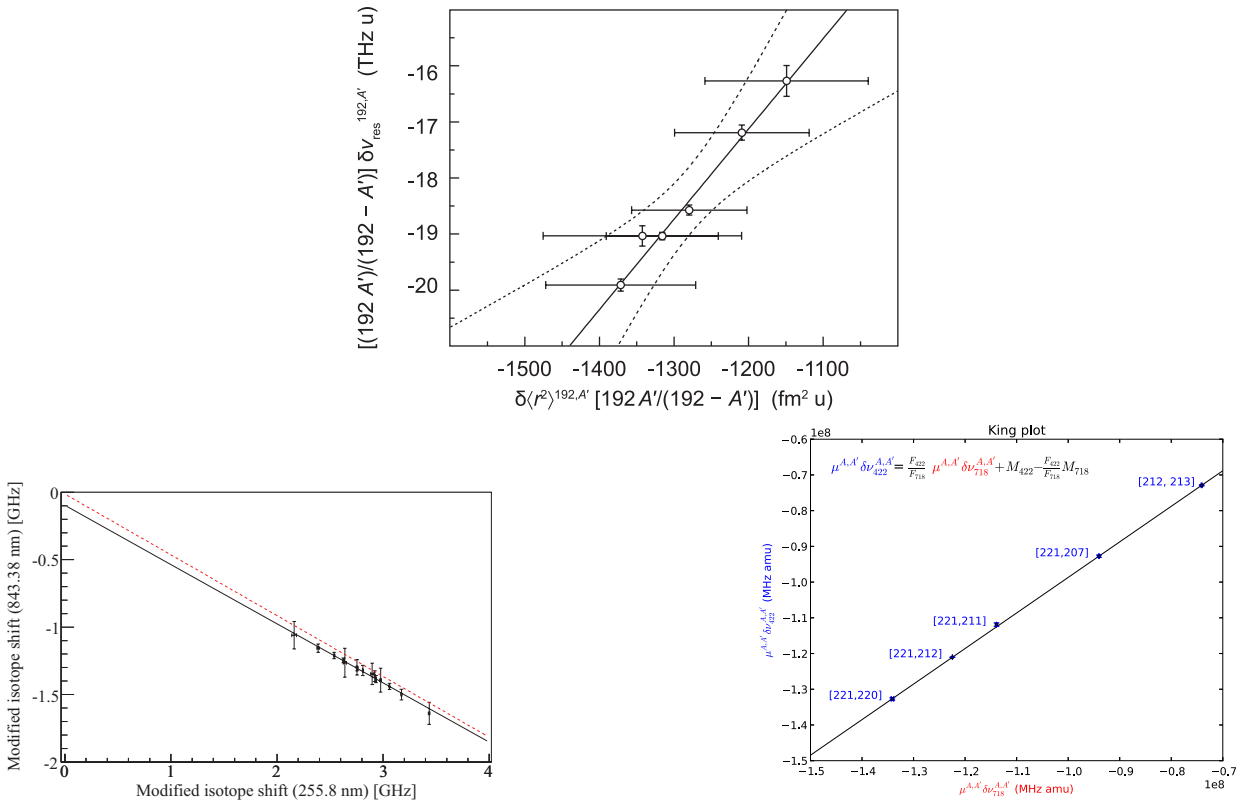

Figure 2.6: Top: example of King plot for extracting the atomic parameters in an atomic transition in osmium [KCA+11]. Bottom: examples of modified King plots to test atomic calculations in polonium (left) [CDS+11, CCF12], and to extract atomic parameters from one transition to another in francium (right) [LBB+14].

Chapter 3

The production of radioactive beams

The lasers have gained in the last few decades a preponderant place in the production of radioactive ion beams. Their activities can be divided into two very broad categories: *let's blast the hell out of this stuff* and *aren't the rainbows the most fabulous things in the world*. The former is based on the use of high-power systems to desorb particles, while the latter is making use of resonant transitions within the atom. For the purpose of these lectures, only the latter cases are being discussed.

3.1 Basics of radioactive ion beam production

Although there are numerous radioactive elements available in the environment, some of which are natural, some of what are man made, most of modern nuclear physics research concentrates on isotopes that are not readily available. Instead, we resort to producing those isotopes are accelerator facilities around the world. Once, two general schools of radioactive ion beam (RIB) production can be considered: the isotope separation on-line (ISOL) technique, and the fragmentation technique.

3.1.1 ISOL

Hot target

At ISOL facilities, a light projectile (typically protons) is sent onto a thick target (e.g. molten metal - Pb, metal foils - Ta, oxides - CaO, carbides - SiC). The radioactive recoils are captured by the target itself and they need to be extracted quickly to be delivered to the experimental setup. This is typically achieved by diffusion, enhanced by maintaining the target unit at high temperature ($\sim 2000°$). Ions are then allowed to diffuse out of the target material and effuse towards a separate ion source.

The time scale for the diffusion and effusion processes varies for one element to the other, and from one target material to the other [LCD+97]. They can be rather long. They vary from a few ms in the most volatile elements to and infinite time (i.e. not being released) for any elements which vapour pressure is higher than that of Fe. In order to extract such

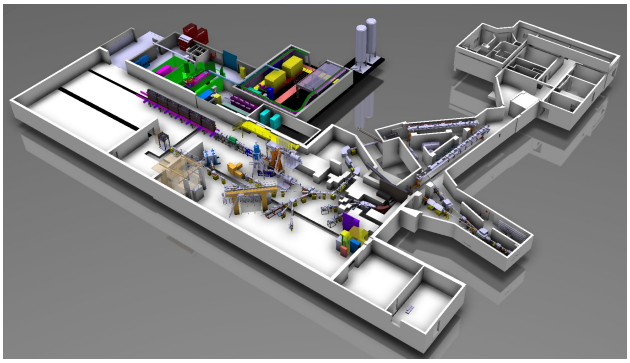

Figure 3.1: CERN ISOLDE, a typical ISOL facility [Kug00].

elements, the needed temperature would result in the melting of the steel out of which the target unit is made. Alternatives methods can be used to extract less volatile elements, such as the use of molecule extraction (e.g. HfF_6 or PoO).

After ionisation, the total beam produced is accelerated by high voltage to $30 - 60\,\mathrm{keV}$ and analysed through a dipole magnet, which provides a A/q separation. Since the beams are mostly 1^+, these are known as *mass separators*. Some 2^+ beams are also sometimes present. These separators allow to provide a single mass beam to the experiment with a rather high beam purity and quality (emittance $< 10\pi\,\mathrm{mm\,mrad}$).

Ion sources

One of the key component of any ISOL facility is the ion source. This is where the radioactive recoils are ionised to be accelerated and further transported to the experiment. The ionisation method is highly dependent upon the chemical property of each element, such as its volatility and, most importantly, its ionisation potential (IP).

Surface For elements with low IP, and typically with their outmost electron loosely bound to the atom, it is sufficient to use a surface ion source. The principle is that when the atom comes in contact with a hot surface, if the work function is suitably matching in energy, the electron will preferentially remain on the hot surface, release the atom in an ionic form.

This process is temperature dependent and the surface ion source is typically maintained at 2000°, well matched with the target temperature.

A small electric field is also created by the voltage drop across the ion source, which is used to heat up the material with high current. This field ensures that the ions converge towards the middle of the source and minimise the recombination of surface ions with electrons.

This type of ion source is very efficient for alkali, alkali-earth, and rare-earth elements. Some random low-IP elements are also available, such as ${}_{31}$Ga and ${}_{81}$Tl.

Plasma For elements with a high IP but nonetheless volatile, a good approach is the electron impact ionisation. It consists in stripping off an electron by using a stream of electrons. The plasma source is made by confining fast moving electrons with a magnetic field and sending the atoms of interest through.

This type of source has a larger emittance than the surface source, partially due to the high excitations around the process. It is a very non-discriminate source, but it relies on the atoms flying in of their own accord. This is therefore best suited for gaseous elements, typically found on the right-hand side of the periodic table of the elements (noble gases, halogen, O).

IGISOL

The general concept of the ISOL technique may also be applied in a slightly modified approach involving a gas cell as the main interaction medium. A projectile is sent on a thin target held inside a noble gas medium. The radioactive nuclei recoil from the target and are caught in the gas. They then thermalise to either a neutral or 1^+ state, drift along the gas flow towards an exit nozzle and are finally ejected and accelerated as in the standard ISOL approach.

3.1.2 Fragmentation

At fragmentation facilities, a heavy projective is sent onto a thin target (e.g. Be) at high energies and broken into all sorts of tiny bits that carry on flying along the path they were on. The beam is then analysed through a series of magnetic and electric dipoles, and in a high charge state. Those beams are typically of very exotic nature, and this production technique does not have any chemical restriction (nor selectivity). It is used for discovery facilities and the study of very exotic species, but not very well suited for the study of the atomic properties of elements.

Some new developments are however underway to couple fragment separators with gas catchers, where the beam can be thermalised and brought to a neutral state, from which the same considerations as for the IGISOL approach (see section 3.1.1) may then be considered.

3.2 Resonance Ionisation Laser Ion Sources

From the ISOL discussion above, it becomes clear that between the surface ion source, which handles the left-hand side of the periodic table, and the plasma source, which deals with the right-hand side, the metals that constitute the middle of the periodic table are unaccessible to ISOL facilities.

This gap has successfully been breached by the use of the resonance ionisation laser ion source (RILIS) as described below.

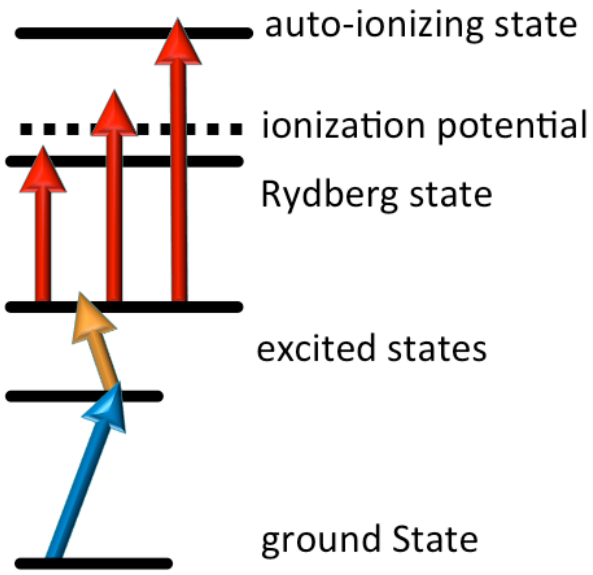

Figure 3.2: General description of a resonance ionisation laser ionisation scheme.

3.2.1 RILIS

The resonance ionisation laser ion source (RILIS) is a technique by which a set of laser beams are sent into the ion source, whereby a valence electron is excited from the ground state of the atom via resonant excitation steps, until the electron is brought beyond the ionisation threshold [FKM12]. The transitions are chosen so that no single laser light has enough energy to non-resonantly excite another element beyond it IP. This results typically in the use of two to three laser beams to excite an element.

There are three modes of operation of a RILIS:

- the final step uses brut force to excite the electron across the ionisation threshold. This is a rather inefficient process and requires a lot of power in the last laser.
- the final step is to an auto-ionising step, whereby two electrons are involved in the creation of an atomic level beyond the ionisation threshold, such that eventually one of the detaches from the atom and the other one recombines into the ion. This process can be very efficient but such levels are not always accessible.
- the final step is to a Rydberg state, a high lying state part of an extended band structure that converges towards the ionisation threshold. Once so close to the ionisation threshold, a small field such as that applied across the ion source is sufficient to ionise the atom.

Note that each element have their own atomic structure, which can be seen as a fingerprint of that element, and the schemes are therefore very selective. The selectivity is a function

of the width of a resonance, Γ, with respect to the separation to the next resonance, $\Delta\omega_{AB}$

$$S = \left(\frac{\Delta\omega_{AB}}{\Gamma} \right)^2 . \tag{3.1}$$

Each resonant transition adds up to the selectivity of the process, so that the total selectivity of a resonant ionisation scheme may be determined as

$$S_{total} = \prod S_i . \tag{3.2}$$

Within an ion source, the selectivity of an element is infinite, as no other element can be sensitive to the choice of resonant transition. (unless you are EXTREMELY unlucky, in which case you should chose another excitation scheme!) There remains however always a background associated with other ionisation mechanisms inherent to the ion source geometry, such as surface ionisation.

This chemical selectivity, coupled with the mass separation capability of the ISOL technique, results in the production of a single isotope beam for the experiments on radioactive ion beams.

Isomeric beams

Using the hyperfine structure defined in section 2.2, it might be possible to resolve the different transitions of different isomers with laser excitation. This approach is limited by the magnitudes of different effects:

- the spread of the transitions in the hyperfine structure depend upon the chosen transition and the nuclear properties. They typically span a few 100 MHz, though some special cases have very small moments that give rise to completely collapsed structures, while some other elements (e.g. $_{29}$Cu, $_{47}$Ag, and many heavy elements) have very wide hyperfine structures spreading over several GHz.

- the width of the resonance is determined mostly by environmental factors, such as the high temperature of the ion source giving rise to several GHz Doppler broadening, or collisions with the buffer gas giving rise to several GHz Lorentz broadening.

In some selected cases, it is nonetheless possible to enhance the ionisation of one isomer over the others of a single isotope, and provide an even cleaner beam for detailed experimental studies [VRGA$^+$04, SGA$^+$07].

LIST

The surface ionisation background from the ion source can be source of problem for some experiments. If both the background nuclei and nuclei of interest are radioactive, decay spectroscopy experiments will have difficult time disentangling the spectrum from each element. For atomic experiment (e.g. mass measurement, laser spectroscopy) and nuclear

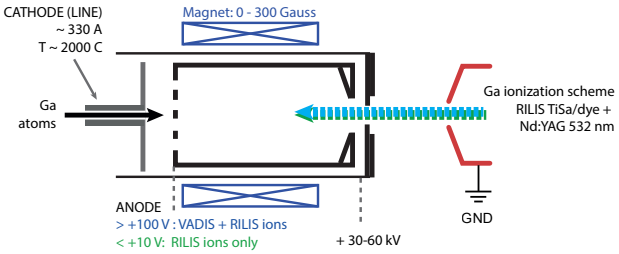

Figure 3.3: Conceptual diagram of the VADLIS ion source.

reaction experiments, those contaminants also saturate the beam and are a hindrance to the experimental programme.

The first approach that may be used to remedy to this situation is to compare the experimental with the lasers ON or OFF. This approach is however limited to the level of purity of the beam. If the nuclei of interest dominate, it is possible to remove the background without damaging too much the signal. If the nuclei of interest are completely buried under the background, the experiment might be in jeopardy.

An extensive programme is ongoing at many ISOL facilities to reduce the sources of non-resonant contamination. Such an approach is the laser ion source and trap (LIST), where the atomisation (hot cavity) is geometrically decoupled from the ionisation region. An electrode is placed in front of the ionisation volume to repel surface ions from being extracted, while a radio-frequency quadrupole is used to confine the laser ions [BGK+03].

This technique has been successfully applied at many facilities [SCG+09, FRB+15], though some issues remain to be addressed, as alternative sources of non-resonant ionisation appeared from the design of these devices [FCA+15].

VADLIS

Another approach that has recently been under investigation is the coupling of the ISOLDE plasma source VADIS with the RILIS. This was never before considered because the geometry of the VADIS ion source does not allow for the lasers to fully irradiate the volume of atoms inside the environment. It was thus deemed a not suitable environment.

The standard geometry of ion source (a small Ta tube) is however incompatible with a molten metal target, as the fumes from the target may condensate on some colder parts of the tube and clog the exit channel. In order to combine the molten metal targets with the RILIS, a research programme was initiated at ISOLDE.

This has resulted in the successful ionisation of Ga and Hg using RILIS in a VADIS ion source, as well as the ion ionisation to Ba^{++}.

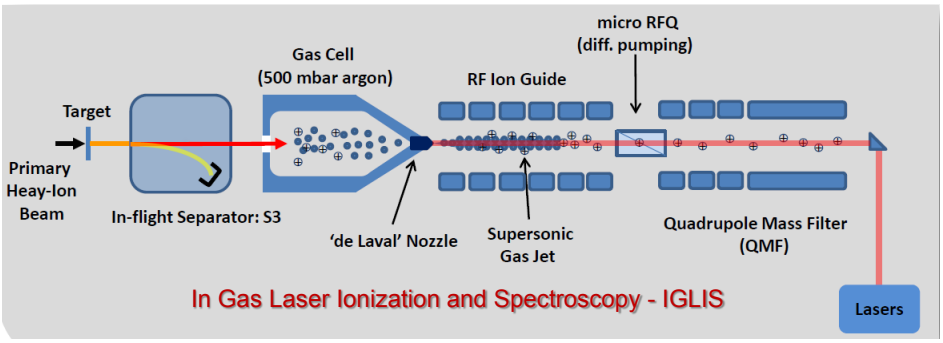

Figure 3.4: Conceptual design of the IGLIS at S3, GANIL.

3.2.2 IGLIS

In-gas laser ionisation and spectroscopy (IGLIS) is the gas-cell variant of the RILIS. In this case, the laser beams are sent into the gas catcher, in the vicinity of the exit nozzle where the atoms are travelling [KFH+03].

Extensive research has been performed by the experimental group in LISOL, Centre de Recherche du Cyclotron in Louvain-La-Neuve, Belgium. The importance of the gas purity [KBH+01, FBD+04] and of the charge density [KCG+09] has been studied in depth, which has resulted in the construction of many new facilities, such as S3 at GANIL, Caen, France [FBB+13].

The typical time required to thermalise the radioactive recoils and transport them with the gas glow to the exit nozzle is of the order of 100 ms. This is far superior to the chemical reaction rates and results in the possible formation of many molecules. While some approach are taken to break down the loosely-bound molecules, some elements are irreversibly attached to others, such as YO. Elements trapped in a molecular form are not accessible to laser ionisation, as the electronic structure of the molecule is completely different of that of the independent elements.

IJLIS

It has already been discussed in section **??** that the linewidth of the resonances in resonance ionisation are limited by the environmental factors, such as the pressure of a gas catcher. This linewidth has a large impact on the selectivity of isomers, for example, or for the application of in-source laser spectroscopy (discussed in the following section).

In order to reduce this effect, a new research programme is ongoing to perform the resonance ionisation in the gas jet outside the gas catcher, rather than in the gas cell itself [SCG+09, KFH+13]. The supersonic gas jet has a a low temperature and is not subject anymore to the pressure broadening that is observed within the gas catcher. The only remnant broadening comes from the divergence of the gas, which can be minimised through the use of a De Laval nozzle (similar to that of a jet engine) and controlling the background pressure in the vessel where the gas cell is located. It's all about rocket science!

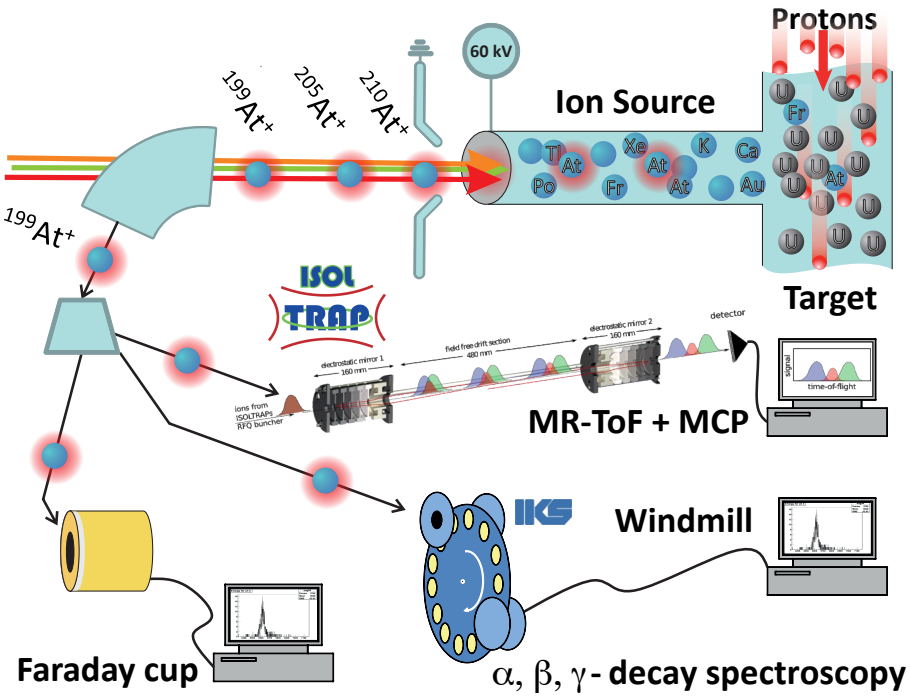

Figure 3.5: In-source laser spectroscopy at CERN ISOLDE. The RILIS source is used to study the hyperfine structure of the isotopes that are detected using a Faraday cup, the ISOLTRAP MR-ToF or the Windmill decay spectroscopy setup.

3.3 In-source laser spectroscopy

Resonance ionisation can be used to explore the nuclear properties of radioactive isotopes via the study of their hyperfine structure, as discussed in section 2.2. By monitoring the ionisation efficiency as a function of the applied frequency of one of the lasers, it is possible to reveal the hyperfine structure of radioactive isotopes, as well as the isotope shift along a chain of isotopes.

Depending on the intensity of the beam, the isobaric contamination, and the presence of isomers, difference approaches are used to determine the ionisation efficiency. Assuming that the overall ion source conditions remain unchanged, it is sufficient to monitor the ion current in a Faraday cup or a micro-channel plate detector, or to record the activity of a sample at a decay spectroscopy station.

At the CERN ISOLDE facility, this technique has been widely applied to study the $_{29}$Cu [FVA^{+}09, KSF^{+}11], $_{82}$Pb [DWAB^{+}07, SAB^{+}09], and $_{84}$Po [CDS^{+}11, SCD^{+}13, SCD^{+}14, FCA^{+}15] isotopes. At the PNPI IRIS facility, Gatchina, Russia, numerous studies are being made, e.g. on the $_{81}$Tl [BBF^{+}12, BBF^{+}13] isotopes. Those two collaborations work closely

with each other and have collected recently numerous data on $_{79}$Au, $_{80}$Hg, $_{81}$Tl, $_{83}$Bi, and $_{85}$At, which are currently under analysis and promise a very thorough discussion of the $Z = 82$ region in the coming years.

At the IGLIS facility LISOL, successful studies of $_{29}$Cu [CAB^{+}09, CAB^{+}10] and $_{47}$Ag [FBC^{+}14] have been made. Those studies pave the way to the study of even more exotic isotopes at the GANIL S3 facility.

Chapter 4

High-resolution collinear laser spectroscopy

In this chapter, we explore the use of high-resolution laser spectroscopy for the study of nuclear properties.

4.1 General concepts

Continuous wave (cw) lasers have a small bandwidth, of the order of several tens of MHz, which are well matched with the natural linewidth of most atomic transitions. They are therefore perfectly suited to study atomic transitions, and sufficient resolution can be reached to address the hyperfine structure and isotope shift, from which the nuclear observables can be determined.

4.1.1 Doppler compression

We have seen, however, that there are also environmental sources of broadening, such as temperature, pressure, or beam divergence. A way to counteract these effects is by accelerating the beam to ISOL energies ($30 - 60\,\mathrm{keV}$). While the environmental perturbations impact on the beam energy distribution, the broadening of the atomic lines is related to the Doppler broadening, which is a function of the velocity. Given the kinetic energy relation

$$E = \frac{1}{2}mv^2 \Rightarrow \delta E = mv\delta v, \tag{4.1}$$

we have that for a constant energy distribution, the velocity distribution is reduced when the velocity is increased. At ISOL facilities, the beam quality is good to start with, and the acceleration voltage is sufficient to reduce the broadening effects to be of the same order of magnitude as the natural linewidth.

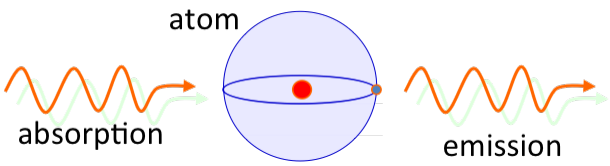

Figure 4.1: Absorption and fluorescence in the atomic nucleus.

4.1.2 Beam bunching

Another important aspect of collinear laser spectroscopy studies is the use of beam bunching. Most of the sources of background in the laser spectroscopy studies are constant in time, such as dark current in the detector or scattered light from the laser. The signal, however, is only proportional to the number of atoms illuminated. As such, if it is possible to compress the atoms in time, it is possible to reduce the background exposure while maintaining the signal.

This is the concept of beam bunching, which is applied through the use of radio-frequency cooler & buncher, which are used to collect the ions coming from the ion source, cool them in a noble buffer gas while confining them in a Paul trap. The ions are finally released in a controlled way, providing a bunch of typical width $1 - 10\,\mu$s every $1 - 100\,$ms, providing up to 10^5 suppression in background exposure.

4.2 Collinear fluorescence

4.2.1 Concept

The basic concept of laser spectroscopy is the absorption of a laser photon by an atom, followed by the emission of photons from the spontaneous decay of the state (see Eq. 2.34). The idea is to repeatedly excite the transition of interest in order to increase the signal from the atom and detect the photons that are emitted via a photomultiplier tube. A clever arrangement of the light collection region can further enhance the signal while trying to minimise the scattered photons from the incoming laser beam.

The incoming ion beam has a high velocity and the laser light will be Doppler shifted in the reference frame of the atom. This characteristic, which can be seen as a hindrance at first, becomes a feature. The aim of laser spectroscopy is to scan the laser frequency. That process can then be taken from two perspectives:

- scan the laser frequency across the resonance correct systematically for the Doppler shift;
- scan the ion beam energy while holding the laser locked on a single frequency using Doppler tuning.

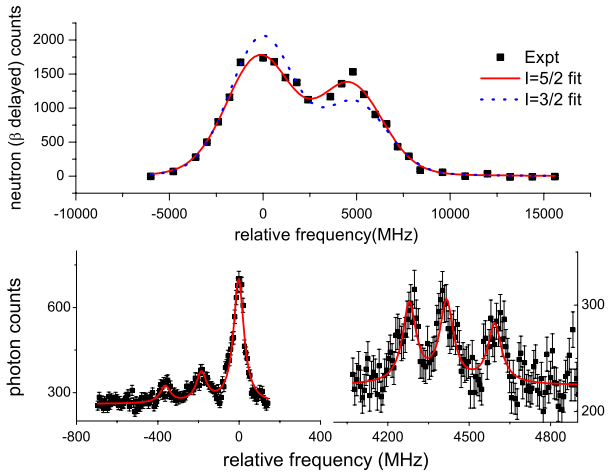

Figure 4.2: Hyperfine spectrum of ^{75}Cu from in-source resonance ionisation and collinear fluorescence laser spectroscopy.

The advantage of the latter system is that great control can be maintained on the laser frequency and on the ion beam energy, hereby minimising the sources of systematic uncertainties. The downside is that the deceleration electrodes may induce beam steering and that they are therefore not appropriate for experiments with long travel path, where the steering effects are amplified.

An important point in the choice of transition is to maximise the number of photons emitted upon interacting with the atom in front of the photomultiplier. This is achieved by choosing a transition with a short lifetime (high Einstein A coefficient in Eq. 2.33) and making sure that it will not contribute to optically pumping the electrons into a dark metastable state.

4.2.2 $_{29}$Cu

A good example of the application of lasers in radioactive ion beam research is the case of the copper isotopes.

Their large hyperfine structure has made it possible to use them for isomeric beam separation, as discussed in section 3.2.1. It has also permitted the study of hyperfine structure in the ion source, e.g. at ISOLDE for ^{75,77}Cu [KSF$^+$11] or at LISOL for ^{57}Cu [CAB$^+$09, CAB$^+$10].

Finally, the copper isotopes have been studied with high resolution laser spectroscopy, see Fig. 4.2. The study of the hyperfine structure has allowed to track the spin and the nuclear orbital contributions to the ground state of the copper isotopes, until it was finally identified that ^{75}Cu$_{46}$ is the isotope where the spherical shell model state of a single $\pi p_{3/2}$ is replaced by an intruder configuration $\pi f_{5/2}$ [FVA$^+$09, VFA$^+$11]. This high-resolution study [VFB$^+$11] also revealed some discrepancy with the gas-catcher work on ^{58}Cu [CAB$^+$10], where the

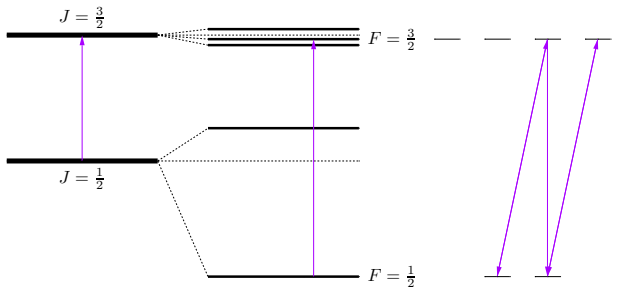

Figure 4.3: Optical pumping in francium with circularly polarised light.

structure was rather collapsed. It points out to the difficulties that may be encountered by the in-source work and that care should be taken with respect to systematic uncertainties from that work.

4.3 Absolute frequency

One of the limitations of laser spectroscopy, especially when studying the lightest isotopes, is that the physics of interest lies below the sensibility of the systematic uncertainty. In the Doppler tuning approach, this is limited by the precision on the ion beam energy, as seen in the Doppler correction relations

$$\nu_- = \nu_0 \sqrt{\frac{1-\beta}{1+\beta}}, \tag{4.2}$$

$$\nu_+ = \nu_0 \sqrt{\frac{1+\beta}{1-\beta}}, \tag{4.3}$$

where $\beta = \frac{v}{c}$ contains the systematic uncertainty from the precision on the acceleration potential as well as the fluctuations and jitter on the power supply. A way to get rid of this uncertainty is to notice that

$$\nu_- \cdot \nu_+ = \nu_0^2. \tag{4.4}$$

so that performing laser spectroscopy in both the collinear and contra linear geometries allows to get rid of the beam energy uncertainties. This approach was used in the study of the $_4$Be isotopes at GSI and ISOLDE [NTŽ+09].

4.4 Polarised beams

Further to the selection rules discussed in section 2.3.2, one may consider the selection rules over the magnetic substates:

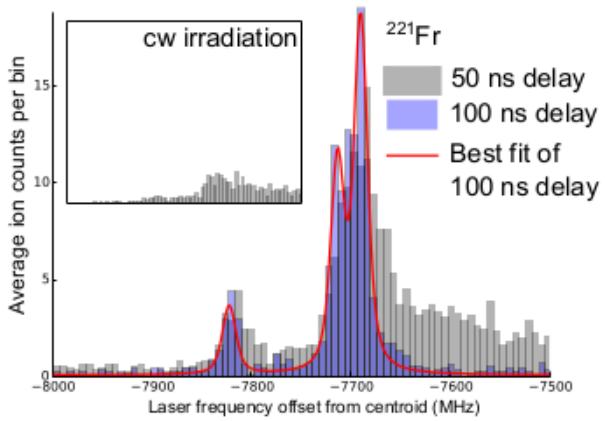

Figure 4.4: Influence of cw light chopping in collinear resonance ionisation spectroscopy of ^{221}Fr [dGBB$^+$15].

$$\text{circular}+ \Rightarrow \Delta m_F = +1, \tag{4.5}$$

$$\text{circular}- \Rightarrow \Delta m_F = -1, \tag{4.6}$$

$$\text{longitudinal} \Rightarrow \Delta m_F = 0. \tag{4.7}$$

Using polarised light, it is therefore possible to manipulate the atomic population so that all the atoms in a bunch occupy the same magnetic substate. By applying a small magnetic field on the path of the atoms, those substates get separated and as the nucleus and the atom are locked together, the orientation of the atom yields to the orientation of the nucleus.

This action provides nuclear polarisation between a few to 100%. By monitoring the asymmetry in the decay of a polarised sample in a crystal lattice, one may determine either the properties of the lattice using a known isotopes, or the properties of the nucleus using a known substrate [Ney03].

This approach has also been applied for the first time in liquid samples recently. This new technical development opens the door to on-line, in-vivo β-NMR studies [GSK$^+$14, SGK$^+$15].

4.5 Collinear resonance

We have seen already that

- resonance ionisation spectroscopy is very efficient, but resolution is limited, see section 3.3;
- collinear fluorescence has high resolution, but its efficiency is limited, by the background and the detection efficiency.

What we really want is to combine the best of both worlds. This is called Collinear Resonance Ionisation Spectroscopy (CRIS), where the high resolution and efficiency are achieved by performing the spectroscopy with resonance ionisation in collinear geometry [KL82].

This, however, also combines the complexity of both techniques, namely:

- bunched, accelerated ion beam, which requires great control of the timing and synchronisation of the experimental equipment;
- high sensitivity to steering effects through the long travel path of the atoms and ions [PAKB$^+$12];
- high number of different lasers: chopped cw laser for the high-resolution transition, pulsed tunable laser for the other resonant transitions, pulsed high-power lasers for the non resonant transitions [CdGB$^+$15];
- need for various sensitive detection systems, including MCP and decay spectroscopy [RLC$^+$13].

In particular, achieving the high resolution is a difficult feature, as the superposition of synchronised high-power lasers together with the cw laser induces two major problems:

- cw light repeated excitation results in optical pumping, and thus loss of signal;
- high-power fields induce power broadening, Stark shift, and a tail to the signal.

In order to overcome these issues, the CRIS collaboration has recently developed the technique of chopped cw light excitation for CRIS, where a Pockels cell is used to change the polarisation of the beam suddenly, and coupled to a polarised beam splitter allows to control the laser beam time structure down to tens of ns [dGBB$^+$15]. This immediately takes away the optical pumping issues, but also allows to shift the synchronisation of the laser beams with respect to each other, so that the high-power laser fields do not overlap, and thus not interact, with the cw laser field.

In the study of ^{219,221}Fr, a peak with full width at half maximum of 30(5) MHz was obtained, which is even better than ever reached for the study of francium by collinear laser spectroscopy.

An observation from this study is that the best suited transition for collinear resonance ionisation spectroscopy has a long lifetime, through which the optical pumping is minimised, and allows for the delaying of the high-power lasers. This means that the Einstein A coefficient must be small (see Eq. 2.33), which is directly opposite to what is required for collinear fluorescence as discussed in section 4.2.1.

Furthermore, the combination of the high resolution and high sensitivity of the CRIS technique with a decay spectroscopy station has allowed to perform decay-assisted laser spectroscopy, as well as laser-assisted decay spectroscopy [LBB$^+$14].

Bibliography

[AAB+02] M. Amoretti, C. Amsler, G. Bonomi, A. Bouchta, P. Bowe, C. Carraro, C. L. Cesar, M. Charlton, M. J. T. Collier, M. Doser, V. Filippini, K. S. Fine, A. Fontana, M. C. Fujiwara, R. Funakoshi, P. Genova, J. S. Hangst, R. S. Hayano, M. H. Holzscheiter, L. V. Jørgensen, V. Lagomarsino, R. Landua, D. Lindelöf, E. Lodi Rizzini, M. Macrì, N. Madsen, G. Manusio, M. Marschsotti, P. Montagna, H. Pruys, C. Regenfus, P. Riedler, J. Rochet, A. Rotondi, G. Rouleau, G. Testera, A. Variola, T. L. Watson, and D. P. van den Werf. Production and detection of cold antihydrogen atoms. *Nature*, 419:456–459, 2002.

[AEG] AEGIS website. http://aegis.web.cern.ch/aegis/.

[ALP] ALPHA website. http://alpha.web.cern.ch/.

[ASA] ASACUSA website. http://asacusa.web.cern.ch/aegis/.

[BBF+12] A. E. Barzakh, L. Kh. Batist, D. V. Fedorov, V. S. Ivanov, K. A. Mezilev, P. L. Molkanov, F. V. Moroz, S. Yu. Orlov, V. N. Panteleev, and Yu. M. Volkov. Hyperfine structure anomaly and magnetic moments of neutron deficient Tl isomers with $I = 9/2$. *Physical Review C*, 86:014311, 2012.

[BBF+13] A. E. Barzakh, L. Kh. Batist, D. V. Fedorov, V. S. Ivanov, K. A. Mezilev, P. L. Molkanov, F. V. Moroz, S. Yu. Orlov, V. N. Panteleev, and Yu. M. Volkov. Changes in the mean-square radii and magnetic moments of neutron-deficient Tl isotopes. *Physical Review C*, 88:024315, 2013.

[BGK+03] K. Blaum, C. Geppert, H.-J. Kluge, M. Mukherjee, S. Schwarz, and K. Wendt. A novel scheme for a highly selective laser ion source. *Nuclear Instruments and Methods B*, 204:331–335, 2003.

[Büt84] S.. Büttgenbach. Magnetic hyperfine anomalies. *Hyperfine Interactions*, 20:1–64, 1984.

[CAB+09] T. E. Cocolios, A. N. Andreyev, B. Bastin, N. Bree, J. Büscher, J. Elseviers, J. Gentens, M. Huyse, Yu. Kudryavtsev, D. Pauwels, T. Sonoda, P. Van den Bergh, and P. Van Duppen. Magnetic dipole moments of ^{57,59}Cu measured by in-gas-cell laser spectroscopy. *Physical Review Letters*, 103:102501, 2009.

[CAB+10] T. E. Cocolios, A. N. Andreyev, B. Bastin, N. Bree, J. Büscher, J. Elseviers, J. Gentens, M. Huyse, Yu. Kudryavtsev, D. Pauwels, T. Sonoda, P. Van den Bergh, and P. Van Duppen. Magnetic dipole moments of ^{57,58,59}Cu. *Physical Review C*, 81:014314, 2010.

[CCF12] B. Cheal, T. E. Cocolios, and S. Fritzsche. Laser spectroscopy of radioactive isotopes: role and limitations of accurate isotope-shift calculations. *Physical Review A*, 86:042501, 2012.

[CdGB+15] T. E. Cocolios, R. P. de Groote, J. Billowes, M. L. Bissell, I. Budinčević, T. Day Goodacre, G. J. Farooq-Smith, V. N. Fedosseev, K. T. Flanagan, S. Franchoo, R. F. Garcia Ruiz, W. Gins, H. Heylen, T. Kron, R. Li, K. M. Lynch, B. A. Marsh, G. Neyens, R. E. Rossel, R. Rothe, A. J. Smith, H. H. Stroke, K. D. A. Wendt, S. G. Wilkins, and X. Yang. High-resolution laser spectroscopy with the collinear resonance ionization spectroscopy (CRIS) experiment at CERN-ISOLDE. *Nuclear Instruments and Methods B*, EMIS Proceedings:submitted, 2015.

[CDS+11] T. E. Cocolios, W. Dexters, M. D. Seliverstov, A. N. Andreyev, S. Antalic, A. E. Barzakh, B. Bastin, J. Büscher, I. G. Darby, D. V. Fedorov, V. N. Fedosseyev, K. T. Flanagan, S. Franchoo, S. Fritzsche, G. Huber, M. Huyse, M. Keupers, U. Köster, Yu. Kudryavtsev, E. Mané, B. A. Marsh, P. L. Molkanov, R. D. Page, A. M. Sjoedin, I. Stefan, J. Van de Walle, P. Van Duppen, M. Venhart, S. G. Zemlyanoy, M. Bender, and P.-H. Heenen. Early onset of ground state deformation in neutron deficient polonium isotopes. *Physical Review Letters*, 106:052503, 2011.

[dGBB+15] R. P. de Groote, I. Budinčević, J. Billowes, M. L. Bissell, T. E.. Cocolios, G. J. Farooq-Smith, V. N. Fedosseev, K. T. Flanagan, S. Franchoo, R. F. Garcia Ruiz, H. Heylen, R. Li, K. M. Lynch, B. A. Marsh, G. Neyens, R. E. Rossel, R. Rothe, H. H. Stroke, K. D. A. Wendt, S. G. Wilkins, and X. Yang. Use of a continuous wave laser Pocles cell for sensitive high-resolution collinear resonance ionization spectroscopy. *Physical Review Letters*, 115:132501, 2015.

[DJS05] V. A. Dzuba, W. R. Johnson, and M. S. Safronova. Calculation of isotope shifts for cesium and francium. *Physical Review A*, 72:022503, 2005.

[DWAB+07] H. De Witte, A. N. Andreyev, N. Barré, M. Bender, T. E. Cocolios, S. Dean, D. Fedorov, V. N. Fedoseyev, L. M. Fraile, S. Franchoo, V. Hellemans, P.-H. Heenen, K. Heyde, G. Huber, M. Huyse, H. Jeppessen, U. Köster, P. Kunz, S. R. Lesher, B. A. Marsh, I. Mukha, B. Roussière, J. Sauvage, M. Seliverstov, I. Stefanescu, E. Tengborn, K. Van de Vel, J. Van de Walle, P. Van Duppen, and Yu. Volkov. Nuclear charge radii of neutron deficient lead isotopes beyond N=104 mid-shell investigated by in-source laser spectroscopy. *Physical Review Letters*, 98:112502, 2007.

[FBB+13] R. Ferrer, B. Bastin, D. Boilley, P. Creemers, P. Delahaye, E. Liénard, X. Fléchard, S. Franchoo, L. Ghys, M. Huyse, Yu. Kudryavtsev, N. Lecesne, H. Lu, F. Lutton, E. Mogilevskiy, D. Pauwels, J. Piot, D. Radulov, L. Rens, H. Savajols, J.-C. Thomas, E. Traykov, C. Van Beveren, P. Van den Bergh, and P. Van Duppen. In gas laser ionization and spectroscopy experiments at the Superconducting Separator Spectrometer (S^3): conceptual studies and preliminary design. *Nuclear Instruments and Methods B*, 317:570–581, 2013.

[FBC+14] R. Ferrer, N. Bree, T. E. Cocolios, I. G. Darby, H. De Witte, W. Dexters, J. Diriken, J. Elseviers, S. Franchoo, M. Huyse, N. Kesteloot, Kudryavtsev Yu., D. Pauwels, D. Radulov, T. Roger, H. Savajols, P. Van Duppen, and M.. Venhart. In-gas-cell laser ionization spectroscopy in the vicinity of ^{100}Sn: magnetic moments and mean-square charge radii of $N = 50 - 54$ Ag. *Physics Letters B*, 728:191–197, 2014.

[FBD+04] M. Facina, B. Bruyneel, S. Dean, J. Gentens, M. Huyse, Yu. Kudryavtsev, P. Van den Bergh, and Van Duppen. A gas cell for thermalizing, storing and transporting radioactive ions and atoms. Part II: on-line studies with a laser ion source. *Nuclear Instruments and Methods B*, 226:401–418, 2004.

[FCA+15] D. A. Fink, T. E. Cocolios, A. N. Andreyev, S. Antalic, A. E. Barzakh, B. Bastin, D. V. Fedorov, V. N. Fedosseev, K. T. Flanagan, L. Ghys, A. Gottberg, M. Huyse, N. Imai, T. Kron, N. Lecesne, K. M. Lynch, B. A. Marsh, D. Pauwels, E. Rapisarda, S. D. Richter, Rossel. R. E., S. Rothe, M. D. Seliverstov, A. M. Sjödin, C. Van Beveren, P. Van Duppen, and K. D. A. Wendt. In-source laser spectroscopy with the laser ion source and trap: First direct study of the ground-state properties of ^{217,219}Po. *Physical Review X*, 5:011018, 2015.

[FH04] G. Fricke and K. Heilig. *Nuclear charge radii*. Springer, 2004.

[FKM12] V. N. Fedosseev, Yu. Kudryavtsev, and V. I. Mishin. Resonance laser ionization of atoms for nuclear physics. *Physica Scripta*, 85:058104, 2012.

[FRB+15] D. A. Fink, S. D. Richter, K. Blaum, R. Catherall, B. Crepieux, V. N. Fedosseev, A. Gottberg, Kron T., B. A. Marsh, C. Mattolat, S. Raeder, R. E. Rossel, S. Rothe, F. Schwellnus, M. D. Seliverstov, M. Sjödin, T. Stora, P. Suominen, and K. D. A. Wendt. On-line implementation and first operation of the Laser Ion Source and Trap at ISOLDE. *Nuclear Instruments and Methods B*, 344:83–95, 2015.

[FVA+09] K. T. Flanagan, P. Vingerhoets, M. Avgoulea, J. Billowes, M. L. Bissell, K. Blaum, B. Cheal, M. De Rydt, V. N. Fedosseev, D. H. Forest, Goeppert Ch., U. Köster, M. Kowalska, J. Krämer, K. L. Kratz, A. Krieger, E. Mané, B. A. Marsh, T. Materna, L. Mathieu, P. L. Molkanov, R. Neugart, G. Neyens,

W. Nörterhäuser, M. D. Seliverstov, O. Serot, Schug. M., M. A. Sjoedin, J. R. Stone, N. J. Stone, H. H. Stroke, G. Tungate, D. T. Yordanov, and Yu. M. Volkov. Nuclear spins and magnetic moments of ^{71,73,75}Cu: inversion of $\pi 2p_{3/2}$ and $\pi 1f_{5/2}$ levels in ^{75}Cu. *Physical Review Letters*, 103:142501, 2009.

[GSK+14] A. Gottberg, M. Stachura, M. Kowalska, M. Bissell, V. Arcisauskaite, K. Blaum, A. Helmke, K. Johnston, K. Kreim, F. H. Larsen, R. Neugart, G. Neyens, R. F. Garcia Ruiz, D. Szunyogh, P. W. Thulstrup, D. T. Yordanov, and L. Hemmingsen. Billion-fold enhancement in sensitivity of nuclear magnetic resonance spectroscopy for magnesium ions in solution. *ChemPhysChem*, 15:3929–3932, 2014.

[KBH+01] Yu. Kudryavtsev, B.. Bruyneel, M. Huyse, J. Gentens, J. Van den Bergh, P. Van Duppen, and L. Vermeeren. A gas cell for thermalizing, storing and transporting radioactive ions and atoms. Part I: off-line studies with a laser ion source. *Nuclear Instruments and Methods B*, 179:412–435, 2001.

[KCA+11] A. Kellerbauer, C. Canali, Fischer A., U. Warring, and S. Fritzsche. Isotope shift of the electric-dipole transition in Os^-. *Physical Review A*, 84:062510, 2011.

[KCG+09] Yu. Kudryavtsev, T. E. Cocolios, J. Gentens, M. Huyse, O. Ivanov, D. Pauwels, T. Sonoda, J. Van den Bergh, and P. Van Duppen. Dual chamber laser ion source at LISOL. *Nuclear Instruments and Methods B*, 267:2908–2918, 2009.

[KFH+03] Yu. Kudryavtsev, M. Facina, M. Huyse, J. Gentens, J. Van den Bergh, and P. Van Duppen. Beams of isotopes produced at LISOL by laser ionization after thermalization of energetic ions in a gas cell. *Nuclear Instruments and Methods B*, 204:336–342, 2003.

[KFH+13] Yu. Kudryavtsev, R. Ferrer, M. Huyse, J. Van den Bergh, and P. Van Duppen. The in-gas-jet laser ion source: resonance ionization spectroscopy of radioactive atoms in supersonic gas jets. *Nuclear Instruments and Methods B*, 297:7–22, 2013.

[KL82] Yu. A. Kudriavtsev and V. S. Lethokov. Laser method of highly selective detection of rare radioactive isotopes through multistep photoionization of accelerator atoms. *Applied Physics B*, 29:219, 1982.

[KSF+11] U. Köster, N. J. Stone, K. T. Flanagan, J. Rikovska Stone, V. N. Fedosseev, K. L. Kratz, B. A. Marsh, T. Maternal, L. Mathieu, P. L. Molkanov, M. D. Seliverstov, O. Serot, A. M. Sjödin, and Yu. M.. Volkov. In-source laser spectroscopy of ^{75,77,78}Cu: direct evidence for a change in the quasiparticle energy sequence in ^{75,77}Cu and an absence of longer-lived isomers in ^{78}Cu. *Physical Review C*, 84:034320, 2011.

[Kug00] E. Kugler. The ISOLDE facility. *Hyperfine Interactions*, 129:23–42, 2000.

[LBB+14] K. M. Lynch, J. Billowes, M. L. Bissell, I. Budinčević, T. E. Cocolios, R. P. de Groote, S. De Schepper, V. N. Fedosseev, K. T. Flanagan, S¿ Frnchoo, R¿ F. Garcia Ruiz, H. Heylen, B. A. Marsh, G. Neyens, T. J. Procter, R. E. Rossel, S. Rothe, I. Strashnov, H. H. Stroke, and K. D. A. Wendt. Decay-assisted laser spectroscopy of neutron-deficient francium. *Physical Review X*, 4:011055, 2014.

[LCD+97] J. Lettry, R. Catherall, P. Drumm, P. Van Duppen, A. H. M. Evensen, G. J. Focker, A. Jokinen, O. C. Jonsson, E. Kugler, H. Ravn, and ISOLDE Collaboration. Pulse shape of the ISOLDE radioactive ion beam. *Nuclear Instruments and Methods B*, 126:130–134, 1997.

[Ney03] G. Neyens. Nuclear magnetic and quadrupole moments for nuclear structure research on exotic nuclei. *Report on Progress in Physics*, 66:633–689, 2003.

[NTŽ+09] W. Nöretchäuser, D. Tiedemann, Z. Žaková, Andjelkovic, K. Blaum, M. L. Bissell, R. Cazan, G. W. F. Drake, Ch. Geppert, M. Kowalska, J. Krämer, A. Krieger, R. Neugart, R. Sánchez, F. Schmidt-Kaler, Z.-C. Yan, D. T. Yordanov, and C. Zimmermann. Nuclear charge radii of ^{7,9,10}Be and the one-neutron halo nucleu ^{11}Be. *Physical Review Letters*, 102:062503, 2009.

[PAKB+12] T. J. Procter, H. Aghaei-Khozani, J. Billowes, M. L. Bissell, F. Le Blanc, B. Cheal, T. E. Cocolios, K. T. Flanagan, H. Hori, T. Kobayashi, D. Lunney, K. M. Lynch, B. A. Marsh, G. Neyens, J. Papuga, M. M. Rajabali, S. Rothe, G. Simpson, A. J. Smith, H. H. Stroke, W. Vanderheijden, and K. Wendt. Development of the CRIS (collinear resonant ionisation spectroscopy) beam line. *Journal of Physics Conference Series*, 381:012070, 2012.

[RLC+13] M. M. Rajabali, K. M. Lynch, T. E. Cocolios, J. Billowes, S. De Schepper, K. Dewolf, K. T. Flanagan, D. Le Blanc, B. A. Marsh, P. J. R. Mason, I. Matea, G. Neyens, J. Papuga, T. J. Procter, S. Rothe, G. S. Simpson, A. J. Smith, H. H. Stroke, D. Verney, P. M. Walker, K. Wendt, and R. T. Wood. A dedicated decay-spectroscopy station for the collinear resonance ionization experiment at ISOLDE. *Nuclear Instruments and Methods B*, 707:35–39, 2013.

[SAB+09] M. D. Seliverstov, A. N. Andreyev, N. Barré, A. E. Barzakh, S. Dean, H. De Witte, D. V. Fedorov, V. N. Fedoseyev, L. M. Fraile, S. Franchoo, J. Genevey, G. Huber, M. Huyse, U. Köster, P. Kunz, S. R. Lesher, B. A. Marsh, I. Mukha, B. Roussière, J. Sauvage, I. Stefanescu, K. Van de Vel, P. Van Duppen, and Yu. M. Volkov. Charge radii and magnetic moments of odd-A $^{183-189}$Pb isotopes. *European Physics Journal A*, 41:315–321, 2009.

[SCD+13] M. D. Seliverstov, T. E. Cocolios, W. Dexters, A. N. Andreyev, S. Antalic, A. E. Barzakh, B. Bastin, J. Büscher, I. G. Darby, D. V. Fedorov, V. N. Fedoseyev, K. T. Flanagan, S. Franchoo, S. ans Fritzsche, G. Huber, M. Huyse,

M. Keupers, U. Köster, Yu. Kudryavtsev, B. A. Marsh, P. L. Molkanov, R. D. Page, A. M. Sjödin, I. Stefan, J. Van de Walle, P. Van Duppen, M. Venhart, and S. G. Zemlyanoy. Charge radii of odd-A $^{191-211}$Po isotopes. *Physics Letters B*, 719:362–366, 2013.

[SCD+14] M. D. Seliverstov, T. E. Cocolios, W. Dexters, A. N. Andreyev, S. Antalic, A. E. Barzakh, B. Bastin, J. Büscher, I. G. Darby, D. V. Fedorov, V. N. Fedosseev, K. T. Flanagan, S. Franchoo, G. Huber, M. Huyse, M. Keupers, U. Köster, Yu. Kudryavtsev, B. A. Marsh, P. L. Molkanov, R. D. Page, A. M. Sjödin, I. Stefan, P. Van Duppen, M. Venhart, and S. Zemlyanoy. Electromagnetic moments of odd-A $^{191-203,211}$Po isotopes. *Physical Review C*, 89:034323, 2014.

[SCG+09] T. Sonoda, T. E. Cocolios, J. Gentians, M. Huyse, O. Ivanov, Yu. Kudryavtsev, D. Pauwels, P. Van den Bergh, and P. Van Duppen. The Laser Ion Source Trap (LIST) coupled to a gas cell catcher. *Nuclear Instruments and Methods B*, 267:2918–2926, 2009.

[Sel69] E. C. Seltzer. k x-ray isotope shifts. *Physical Review*, 188:1916–1919, 1969.

[SGA+07] I. Stefanescu, G. Georgiev, F. Ames, J. Äyetö, D. Balabanski, G. Bollen, P. A. Butler, J. Cederkäll, N. Champault, T. Davinson, A. De Maesschalck, P. Delahaye, J. Eberth, D. Fedorov, V. N. Fedosseev, L. M. Fraile, S. Franchoo, K. Gladnishki, D. Habs, K. Heyde, M. Huyse, O. Ivanov, J. Iwanicki, J. Jolie, B. Jonson, Th. Kröll, R. Krücken, O. Kester, A. Lagoyannis, L. Liljeby, G. Lo Bianco, B. A. Marsh, O. Niedermaier, T. Nilsson, M. Oinonen, G. Pascovici, P. Reiter, A. Saltarelli, D. Scheit, H. ans Schwalm, T. Sieber, N. Smirnova, J. Van de Walle, P. Van Duppen, S. Zemlyanoi, N. Warr, D. Weisshaar, and F. Wenander. Coulomb excitation of ^{68,70}Cu: First use of post-accelerated isomeric beams. *Physical Review Letters*, 98:122701, 2007.

[SGK+15] M. Stachura, A. Gottberg, M. Kowalska, K. Johnston, and L. Hemmingsen. Towards applications of β-NMR spectroscopy in chemistry and biochemistry. *Nuclear Physics News*, 25:25–29, 2015.

[VFA+11] P. Vingerhoets, K. T. Flanagan, M. Avgoulea, J. Billowes, M. L. Bissell, K. Blaum, B. A. Brown, B. Cheal, M. De Rydt, D. H. Forest, Ch. Geppert, M. Honma, M. Kowalska, J. Krämer, A. Krieger, E. Mané, R. Neugart, G. Neyens, W. Nörteräuser, T. Otsuka, M. Schug, H. H. Stroke, G. Tungate, and D. T. Yordanov. Nuclear spins, magnetic moments, and quadrupole moments of Cu isotopes from $N = 28$ to $N = 46$: probes for core polarization effects. *Physics Letters B*, 703:34–39, 2011.

[VFB+11] P. Vingerhoets, K. T. Flanagan, J. Billowes, M. L. Bissell, K. Blaum, B. Cheal, M. De Rydt, D. H. Forest, Ch. Geppert, M. Honma, M. Kowalska, J. Krämer, K. Kreim, A. Krieger, R. Neugart, G. Neyens, W. Nörteräuser, J. Papuga, T. J.

Procter, M. M. Rajabali, R. Sánchez, H. H. Stroke, and D. T. Yordanov. Magnetic and quadrupole moments of neutron deficient $^{58-62}$Cu isotopes. *Physics Letters B*, 703:34–39, 2011.

[VRGA$^+$04] J. Van Roosbroeck, C. Guénaut, G. Audi, D. Beck, K. Blaum, G. Bollen, J. Cederkall, P. Delahaye, A. De Maesschalck, H. De Witte, D. Fedorov, V. N. Fedosseyev, S. Franchoo, H. O. U. Fynbo, M. Górska, F. Herfurth, K. Heyde, M. Huyse, A. Kellerbauer, H.-J. Kluge, U. Köster, K. Kruglov, D. Lunney, V. I. Mishin, W. F. Mueller, Sz. Nagy, S. Schwarz, L. Schweikhard, N. A. Smirnova, K. Van de Vel, P. Van Duppen, A. Van Dyck, W. B. Walters, L. Weissman, and C. Yazidjian. Unambiguous identification of three β-decaying isomers in ^{70}Cu. *Physical Review Letters*, 92:112501, 2004.